A spreadsheet-based redox flow battery cell cycling model enabled by closed-form approximations

Bertrand J. Neyhouse and Fikile R. Brushett*

Joint Center for Energy Storage Research, Massachusetts Institute of Technology, Cambridge, MA 02139
Department of Chemical Engineering, Massachusetts Institute of Technology, Cambridge, MA 02139
** Corresponding author: brushett@mit.edu*

Abstract

The complex interplay between numerous parasitic processes—voltage losses, crossover, decay—challenges interpretation of cycling characteristics in redox flow batteries (RFBs). Mathematical models offer a means to predict cell performance prior to testing and to interpret experimentally measured cycling data, however most implementations require extensive domain knowledge and computational resources. To address these challenges, we previously developed a computationally inexpensive zero-dimensional modeling approach by deriving analytical solutions to species mass balances during cell cycling. Here, we expand on this framework by deriving closed-form expressions for key performance metrics and comparing the accuracy of these simplifications to the complete analytical model. The resulting closed-form model streamlines the computational structure and allows for spreadsheet modeling of cell cycling behavior, which we highlight by developing a simulation package in Microsoft® Excel®. We then apply this model to analyze previously published experimental data from our group and others, highlighting its utility in numerous diagnostic configurations—bulk electrolysis, compositionally unbalanced symmetric cell cycling, and full cell cycling. Given the accessibility of this modeling toolkit, it has potential to be a widely deployable tool for RFB research, aiding in data interpretation, performance prediction, and electrochemistry education.

Keywords: Redox flow batteries, zero-dimensional models, spreadsheet models, electrochemical engineering, energy storage

Introduction

Redox flow battery (RFB) materials research, a blossoming field at the intersection of chemistry, materials science, and chemical engineering, is expanding the limits of cell performance through the development of new redox species, electrodes, and membranes.[1–7] Within the suite of field-standard characterization approaches—including material property analyses,[8] ex situ electrochemical testing,[9–12] and cell polarization[13,14]—cell cycling is a crucial performance benchmark, yielding quantitative measures of the device efficiency and lifetime. Although these experiments offer critical insights, cell cycling characteristics are often obscured by numerous competing processes—voltage losses, species decay,[4] crossover[15,16]—that challenge interpretation of experimental results (e.g., cycling efficiency, charge/discharge capacity). Further, laboratory-scale testbeds require considerable material quantities and time investments, frustrating systematic investigations into variable operating conditions that are needed to decouple competing effects. While there are indeed advanced diagnostic approaches for isolating individual contributions to performance loss,[17–19] these still require additional resources and may not translate directly to cycling characteristics in a full cell configuration.

Mathematical models offer a means to establish connections between material properties and cell performance, enabling qualitative and quantitative interpretation of cycling data as well as performance predictions.[20,21] Indeed, numerous models have been reported in the open literature, spanning various levels of complexity and dimensionality. However, simulation packages and coding libraries are not always freely available and often require extensive user knowledge in the programming language or multiphysics software (e.g., COMSOL), potentially limiting their appeal to those conducting experimental research. Zero-dimensional models are particularly attractive for simulating extended cycling, as the modeling frameworks rely on coupled systems

of ordinary differential equations—as opposed to higher-dimensional partial differential equations—enabling reduced computation time and resource requirements as compared to more complex representations.[19,22–34] In general, such models neglect spatial variations in species concentrations by assuming the electrolytes in either half-cell are well-mixed domains, sacrificing microscopic granularity for solvability. Even with these simplifications, previous zero-dimensional models have shown good agreement with experimental cycling results, allowing informed predictions of performance metrics and enabling parameter estimation from experimental data.[19,24,26] However, many implementations remain computationally expensive (ca. 30–120 s per cycle on a typical laptop computer),[22,26,33] as the numerical methods required to solve coupled differential equations over tens to hundreds of cycles can lead to hours of computation time for a single set of conditions.

To address this limitation, we previously reported a zero-dimensional modeling framework that leveraged analytical solutions to the species mass balances, reducing simulation times by several orders of magnitude (ca. 0.05 s per cycle) while still retaining quantitative accuracy compared with experimental cycling performance.[23] While this framework supports more extensive evaluations of the interconnections between component material properties and cell cycling performance, it still requires some computational knowledge for proper implementation. Specifically, as exponential decay terms introduce nonlinearities in the mass balance solution, the zero-dimensional model leverages nonlinear algebraic solvers and numerical integration to compute cycle times and efficiencies. These routines only account for ca. 10% of total simulation time but can frustrate model usability and may slow more time-intensive analytical routines (e.g., optimization, controls). To overcome this limitation, exponential terms may be approximated through Taylor expansions to yield polynomial equations for the mass balance solutions, which,

in turn, can be transformed into closed-form analytical expressions for capacities and efficiencies. Indeed, Silcox et al. used an analogous approach for deriving capacity retention with varying redox species decay rates and bulk electrolysis conditions, providing closed-form expressions for predicting capacity fade characteristics under different testing regimes.[27] By extending this methodology to a more generalized zero-dimensional framework, we aim to derive analytical expressions for capacity fade and cycling efficiencies that incorporate common parasitic processes (i.e., crossover, species decay) and sources of voltage losses (i.e., kinetic, ohmic, mass transport). From this model, key performance indicators can be calculated using compact matrix operations, making simulations possible with less complex numerical methods.

To this end, we expand on the analytical zero-dimensional framework by deriving approximations to the mass balances, enabling fully closed-form solutions for cell cycling. Specifically, we apply Taylor expansions to approximate exponential terms in the mass balances as polynomials, facilitating algebraic solutions for charge and discharge times. By incorporating these polynomials into expressions for the cell voltage, we also derive analytical expressions for cell voltaic efficiency. First, to more rigorously characterize the accuracy of the closed-form expressions, we evaluate varying orders of expansion (i.e., first-, second-, and third-order) and compare the root-mean-square error (RMSE) against the full zero-dimensional model. Second, to further accessibility, we develop a spreadsheet model in Microsoft® Excel®, that may form the basis of a flexible and easy-to-use simulation tool for the RFB community. Third, we apply this model to retrospectively analyze previously published cell cycling data from our group and others, demonstrating its ability to predict and/or interpret experimental data and highlighting opportunities for further modification. Ultimately, this work aims to expand the utility of zero-dimensional RFB models, facilitating their use in a wider range of experimental and modeling

studies. Further, the availability of easy-to-use spreadsheet models may support efforts to educate new entrants to the RFB field.

Theoretical framework

The closed-form constitutive equations developed here are derived from simplifications to the generalized zero-dimensional model presented in reference [23]. The model assumes the active species in each half-cell undergo one-electron transfer between their charged and discharged states as shown by **Equation (1)**.

$$\begin{aligned} A &\rightleftharpoons A^{+} + e^{-} \\ B^{+} + e^{-} &\rightleftharpoons B \end{aligned} \tag{1}$$

Species A and B^{+} represent the discharged species in the positive and negative half-cells, respectively, while A^{+} and B represent the corresponding charged species. The ionic charge of each species j (z_j) is such that $z_{A^{+}} = z_A + 1$ and $z_{B^{+}} = z_B + 1$. We assume here that both half-cells are distinct, well-mixed domains, treating the faradaic reactions at the electrode, species decay, and membrane crossover as occurring uniformly throughout the electrolyte volume. Consistent with typical experimental methods, we apply galvanostatic cycling with the same current magnitude applied during charge and discharge. Throughout, we make the following additional assumptions: (1) all processes occur at constant temperature and (2) operating conditions, electrolyte/material properties, and cell characteristics remain constant throughout cycling. All other assumptions are described within the context of the relevant model equations.

***Zero-dimensional flow cell model*—**The general zero-dimensional mass balances are given by **Equation (2)** and subject to the initial condition given by **Equation (3)**.

$$\frac{dC_j^{\infty,h}}{dt} = \pm\frac{I}{V^h F} + \sum R_j^h \tag{2}$$

$$C_j^{\infty,h}\left(t=0\right) = C_j^{o,h} \tag{3}$$

$C_j^{\infty,h}$ (mol m^{-3}) is the bulk concentration of species j in half-cell h, t (s) is the time measured from the beginning of the half-cycle (i.e., charge or discharge), I (A) is the applied current (defined as positive for charge and negative for discharge), V^h (m^3) is the electrolyte volume in half-cell h, F (96,495 C mol^{-1}) is the Faraday constant, R_j^h (mol m^{-3} s^{-1}) represents first-order source and sink terms (i.e., species decay, crossover), $C_j^{o,h}$ (mol m^{-3}) is the initial concentration of species j in half-cell h at the beginning of the half-cycle.

As described by Silcox et al., species decay is assumed to proceed through two homogeneous mechanisms—irreversible decomposition and reversible self-discharge—shown by **Equations (4)** and **(5)**, respectively.[27]

$$\begin{aligned} A^+ &\xrightarrow{\left(1-f_{A^+}\right)k_{d,A^+}} D \\ B &\xrightarrow{(1-f_B)k_{d,B}} D \end{aligned} \tag{4}$$

$$\begin{aligned} A^+ &\xrightarrow{f_{A^+}k_{d,A^+}} A \\ B &\xrightarrow{f_B k_{d,B}} B^+ \end{aligned} \tag{5}$$

$k_{d,j}$ (s^{-1}) is the decay rate constant for species j and f_j is the fraction of species j that decays via self-discharge. Crossover rate constants (**Equation (6)**) are derived from the steady-state flux through the membrane,[17,23] accounting for diffusion, migration, and electro-osmosis and assuming the species flux is positive for transport from the negative electrolyte to the positive electrolyte.

$$k_{c,j}^{-} = \frac{A_m D_j^m K_j}{l_m V^+}\left(\frac{\gamma_j \exp\left(\gamma_j\right)}{\exp\left(\gamma_j\right)-1}\right)$$
$$k_{c,j}^{+} = \frac{A_m D_j^m K_j}{l_m V^+}\left(\frac{\gamma_j}{\exp\left(\gamma_j\right)-1}\right) \quad (6)$$
$$\gamma_j = -\left(\frac{z_j F}{\sigma_m RT} + \frac{\xi}{\lambda C_{\text{site}} D_j^m F}\right)\frac{I l_m}{A_m}$$

$k_{c,j}^{h}$ (s^{-1}) is the crossover rate constant for species j in half-cell h, A_m (m^2) is the geometric membrane area, D_j^m (m^2 s^{-1}) is the diffusion coefficient of species j in the membrane, K_j (dimensionless) is the partition coefficient of species j in the membrane, l_m (m) is the swollen membrane thickness, γ_j (dimensionless) is a parameter scaling electro-osmosis and migration to diffusion for species j, σ_m (S m^{-1}) is the membrane conductivity, R (8.314 J mol^{-1} K^{-1}) is the universal gas constant, T (K) is the absolute temperature, ξ (dimensionless) is the electro-osmostic coefficient, λ (dimensionless) is the molar ratio of solvent to fixed ion sites in the membrane, and C_{site} (mol m^{-3}) is the concentration of fixed ion sites within the membrane.

The cell voltage as a function of time is given by **Equation (7)**, which accounts for the difference in formal redox potentials between the positive and negative redox couples—$E^{0,+}$ (V) and $E^{0,-}$ (V), respectively—ohmic losses, and mass transport losses. Although not considered explicitly here, kinetic losses may also be integrated by considering them as constant resistances—similar to ohmic losses—as discussed in reference [23].

$$E_{cell} = E^{0,+} - E^{0,-} + I\left(R_m + R_c\right) - \frac{RT}{F}\ln\left(\frac{C_A^s C_{B^+}^s}{C_{A^+}^s C_B^s}\right) \quad (7)$$

R_m (Ω) is the membrane resistance, R_c (Ω) represents additional contact resistances, and C_j^s (mol m^{-3}) is the surface concentration of species j at the electrode. Surface concentrations can be

related to the bulk concentration using an advective mass transfer coefficient, $k_{m,j}$ (m s^{-1}), and the accessible electrode surface area, A_{ed} (m^2) according to **Equation (8)**.

$$C_j^s = C_j^\infty \pm \frac{I}{FA_{ed}k_{m,j}} \tag{8}$$

In this work, we consider the product of the mass transfer coefficient and electrode area ($A_{ed}k_{m,j}$) as an input parameter to the model; however, in some instances, $k_{m,j}$ can be predicted from empirical correlations[35–37] while A_{ed} can be measured experimentally.[38]

***Deriving closed-form approximations*—**Incorporating the source and sink terms into the conservation equations for each species, the general mass balances can be written explicitly as **Equation (9)** and simplified to vector-matrix notation in **Equations (10)** and **(11)**.

$$\frac{d}{dt}\begin{bmatrix} C_A^{\infty,+} \\ C_{A^+}^{\infty,+} \\ C_{B^+}^{\infty,+} \\ C_B^{\infty,-} \\ C_{B^+}^{\infty,-} \\ C_A^{\infty,-} \end{bmatrix} = \begin{bmatrix} -\frac{I}{V^+F} \\ \frac{I}{V^+F} \\ 0 \\ \frac{I}{V^-F} \\ -\frac{I}{V^-F} \\ 0 \end{bmatrix} - \begin{bmatrix} k_{c,A}^+ & -f_{A^+}k_{d,A^+} & 0 & -k_{c,B}^- & 0 & -k_{c,A}^- \\ 0 & k_{d,A^+}+k_{c,A^+}^+ & 0 & k_{c,B}^- & 0 & 0 \\ 0 & 0 & k_{c,B^+}^+ & -k_{c,B}^- & k_{c,B^+}^- & 0 \\ 0 & \frac{V^+}{V^-}\left(k_{c,A^+}^+\right) & 0 & k_{d,B}+\frac{V^+}{V^-}\left(k_{c,B}^-\right) & 0 & 0 \\ 0 & -\frac{V^+}{V^-}\left(k_{c,A^+}^+\right) & -\frac{V^+}{V^-}\left(k_{c,B^+}^+\right) & -f_Bk_{d,B} & \frac{V^+}{V^-}\left(k_{c,B^+}^-\right) & 0 \\ -\frac{V^+}{V^-}\left(k_{c,A}^+\right) & -\frac{V^+}{V^-}\left(k_{c,A^+}^+\right) & 0 & 0 & 0 & \frac{V^+}{V^-}\left(k_{c,A}^-\right) \end{bmatrix} \begin{bmatrix} C_A^{\infty,+} \\ C_{A^+}^{\infty,+} \\ C_{B^+}^{\infty,+} \\ C_B^{\infty,-} \\ C_{B^+}^{\infty,-} \\ C_A^{\infty,-} \end{bmatrix} \tag{9}$$

$$\frac{d}{dt}\mathbf{C} = \mathbf{b} - \mathbf{K}\mathbf{C} \tag{10}$$

$$\mathbf{C}(t=0) = \mathbf{C^o} \tag{11}$$

C (mol m^{-3}) is a column vector containing the 6 bulk species concentrations, **b** (mol m^{-3} s^{-1}) is a column vector containing the constant reaction rate terms, **K** (mol m^{-3} s^{-1}) is a matrix containing first-order reaction rate constants, and $\mathbf{C^o}$ (mol m^{-3}) is a column vector containing the initial concentrations. The analytical solution to these mass balances is shown in **Equation (12)**.

$$\mathbf{KC} = \mathbf{b} - \exp\left(-\mathbf{K}t\right)\left(\mathbf{b} - \mathbf{KC}^{\mathbf{o}}\right) \tag{12}$$

Under conditions where the timescales for crossover, species decay, and self-discharge are low relative to the charge and discharge times—that is, $t_c k_i << 1$, $t_d k_i << 1$, where t_c (s) and t_d (s) are the charge and discharge times, respectively, and k_i (s^{-1}) represents a decay or crossover rate constant—the exponentials can be approximated by a Taylor expansion according to **Equation (13)**.

$$\exp\left(-\mathbf{K}t\right) = \sum_{n=0}^{\infty} \frac{\left(-\mathbf{K}t\right)^n}{n!} = 1 - \mathbf{K}t + \frac{1}{2}\left(\mathbf{K}t\right)^2 - \frac{1}{6}\left(\mathbf{K}t\right)^3 + \cdots \tag{13}$$

Here, n is the summation index. In the complete analytical solution, solving **Equation (12)** for the charge and discharge times requires numerical methods, as the sum of exponential terms is nonlinear. By approximating these terms as polynomials, the charge and discharge times can instead be derived algebraically. Generally, higher-order polynomials provide more accurate solutions but increase mathematical complexity; to this end, we derive solutions for first-, second-, and third-order approximations.

***First-order expansions*—**A first-order Taylor expansion of the exponential terms yields the solution to the mass balances given by **Equation (14)**.

$$\mathbf{C} = \mathbf{C}^{\mathbf{o}} + \left(\mathbf{b} - \mathbf{KC}^{\mathbf{o}}\right)t \tag{14}$$

The charge and discharge times are defined by the minimum time required for the reacting species concentrations to reach zero at the electrode surface. For the charging half-cycle, the reacting species are A or B^+, which respectively correspond to the first and fifth elements of **C**. Therefore, the charge time is the result of matrix operations corresponding to those species as given by **Equation (15)**.

$$t_c = \min\left\{\begin{array}{l} -\left(C_A^{o,+} - \dfrac{I}{FA_{ed}k_m}\right)\left(\dfrac{I}{V^+F} - k_{c,A}^+ C_A^{o,+} + f_{A^+}k_{d,A^+}C_{A^+}^{o,+} + k_{c,B}^- C_B^{o,-} + k_{c,A}^- C_A^{o,-}\right)^{-1} \\ -\left(C_{B^+}^{o,-} - \dfrac{I}{FA_{ed}k_m}\right)\left(\dfrac{I}{V^-F} + k_{c,A^+}^+ C_{A^+}^{o,+} + k_{c,B^+}^+ C_{B^+}^{o,+} + f_B k_{d,B} C_B^{o,-} - k_{c,B^+}^- C_{B^+}^{o,-}\right)^{-1} \end{array}\right\} \quad (15)$$

Similarly, the discharge time is given by **Equation (16)**. Note that during discharge, the current is negative by definition.

$$t_d = \min\left\{\begin{array}{l} -\left(C_{A^+}^{o,+} + \dfrac{I}{FA_{ed}k_m}\right)\left(\dfrac{I}{V^+F} - \left(k_{d,A^+} + k_{c,A^+}^+\right)C_{A^+}^{o,+} - k_{c,B}^- C_B^{o,-}\right)^{-1} \\ -\left(C_B^{o,-} + \dfrac{I}{FA_{ed}k_m}\right)\left(\dfrac{I}{V^-F} - k_{c,A^+}^+ C_{A^+}^{o,+} - \left(k_{d,B} + k_{c,B}^-\right)C_B^{o,-}\right)^{-1} \end{array}\right\} \quad (16)$$

As we assume galvanostatic operation, the coulombic efficiency, CE, can be expressed from the charge and discharge times according to **Equation (17)**.

$$\mathrm{CE} = \frac{t_d}{t_c} \quad (17)$$

Determining the voltaic efficiency, VE, requires integration of the cell voltage to determine the average charge and discharge voltage—$\overline{E}_c$ (V) and $\overline{E}_d$ (V), respectively—as shown in **Equation (18)**.

$$\mathrm{VE} = \frac{\overline{E}_d}{\overline{E}_c} = \frac{\dfrac{1}{t_d}\displaystyle\int_0^{t_d}\left(E_{cell}\right)dt}{\dfrac{1}{t_c}\displaystyle\int_0^{t_c}\left(E_{cell}\right)dt} \quad (18)$$

As the derivations are identical for charge and discharge, here we focus on the discharge voltage, written explicitly in **Equation (19)**.

$$\overline{E}_d = \frac{1}{t_d}\int_0^{t_d}\left(E^{0,+} - E^{0,-} + I\left(R_m + R_c\right) - \frac{RT}{F}\ln\left(\frac{\left(C_A^s\right)\left(C_{B^+}^s\right)}{\left(C_{A^+}^s\right)\left(C_B^s\right)}\right)\right)dt \quad (19)$$

As the first several terms are assumed constant over the half-cycle, their integrals are comparatively straightforward as shown in **Equation (20)**.

$$\frac{1}{t_d}\int_0^{t_d}\left(E^{0,+}-E^{0,-}+I\left(R_m+R_c\right)\right)dt = E^{0,+}-E^{0,-}+I\left(R_m+R_c\right) \tag{20}$$

The logarithmic concentration terms are more complex, as each surface concentration is given by a polynomial expression. The integral can be simplified by separating the logarithmic terms (**Equation (21)**) and solved generally according to **Equation (22)** for a first-order expansion.

$$-\frac{RT}{Ft_d}\int_0^{t_d}\left(\ln\left(\frac{\left(C_A^s\right)\left(C_{B^+}^s\right)}{\left(C_{A^+}^s\right)\left(C_B^s\right)}\right)\right)dt = -\frac{RT}{Ft_d}\int_0^{t_d}\left(\ln\left(C_A^s\right)+\ln\left(C_{B^+}^s\right)-\ln\left(C_{A^+}^s\right)-\ln\left(C_B^s\right)\right)dt \tag{21}$$

$$\int_0^X \ln\left(Y+Zt\right)dt = \left(X+\frac{Y}{Z}\right)\ln\left(Y+ZX\right)-X-\frac{Y}{Z}\ln\left(Y\right) \tag{22}$$

Here, *X, Y,* and *Z* are constants representing the linear time dependence of each surface concentration. The integral for each species concentration can then be combined with **Equation (20)** to yield a complete closed-form expression for the discharge voltage. Finally, the energy efficiency, EE, is the product of CE and VE as given in **Equation (23)**.

$$\mathrm{EE} = \mathrm{VE}\times\mathrm{CE} \tag{23}$$

Second-order expansions—For the second-order expansion (**Equation (24)**), we follow the same procedure except that the quadratic formula is used to solve the resulting polynomials.

$$\mathbf{C} = \mathbf{C^o}+\left(\mathbf{b}-\mathbf{KC^o}\right)t-\frac{1}{2}\left(\mathbf{Kb}-\mathbf{K^2C^o}\right)t^2 \tag{24}$$

$$t_c = \min\left\{\begin{array}{ll} \dfrac{-x_2 - \sqrt{(x_2)^2 - 4x_1x_3}}{2x_1}; & x_1 = C_A^{o,+} - \dfrac{I}{FA_{ed}k_m} \\ & x_2 = \mathbf{b_1} - \mathbf{K_{1,*}C^o} \\ & x_3 = \mathbf{K_{1,*}b_1} - \mathbf{K_{1,*}^2C^o} \\ \dfrac{-x_2 - \sqrt{(x_2)^2 - 4x_1x_3}}{2x_1}; & x_1 = C_{B^+}^{o,+} - \dfrac{I}{FA_{ed}k_m} \\ & x_2 = \mathbf{b_5} - \mathbf{K_{5,*}C^o} \\ & x_3 = \mathbf{K_{5,*}b_5} - \mathbf{K_{5,*}^2C^o} \end{array}\right\} \tag{25}$$

$$t_d = \min\left\{\begin{array}{ll} \dfrac{-x_2 - \sqrt{(x_2)^2 - 4x_1x_3}}{2x_1}; & x_1 = C_{A^+}^{o,+} + \dfrac{I}{FA_{ed}k_m} \\ & x_2 = \mathbf{b_2} - \mathbf{K_{2,*}C^o} \\ & x_3 = \mathbf{K_{2,*}b_1} - \mathbf{K_{2,*}^2C^o} \\ \dfrac{-x_2 - \sqrt{(x_2)^2 - 4x_1x_3}}{2x_1}; & x_1 = C_B^{o,+} + \dfrac{I}{FA_{ed}k_m} \\ & x_2 = \mathbf{b_4} - \mathbf{K_{4,*}C^o} \\ & x_3 = \mathbf{K_{4,*}b_4} - \mathbf{K_{4,*}^2C^o} \end{array}\right\} \tag{26}$$

Here, x_1, x_2, and x_3 (s) are constants. The vector subscripts indicate individual elements, with the asterisk indicating a row of the corresponding matrix. Interestingly, the lower root of the quadratic approximation always corresponds to the charge / discharge times, as the parabolic concentration-time function for the reacting species is concave upward. The higher root corresponds to non-physical conditions where concentrations fall below zero or grow unrealistically large. Computing the VE requires integration of the logarithms, which now feature second-order polynomials. The general form of this integral is given by **Equation (27)**.

$$\int_0^W \ln\left(X + Yt + Zt^2\right)dt = \left[\begin{array}{l} \dfrac{\sqrt{Y^2 - 4XZ}}{2Z}\left(\ln\left(\dfrac{2ZW + Y + \sqrt{Y^2 - 4XZ}}{Y + \sqrt{Y^2 - 4XZ}}\right) - \ln\left(\dfrac{2ZW + Y - \sqrt{Y^2 - 4XZ}}{Y - \sqrt{Y^2 - 4XZ}}\right)\right) \\ + \left(\dfrac{Y}{2Z} + W\right)\log\left(X + YW + ZX^2\right) - \left(\dfrac{Y}{2Z}\right)\log\left(X\right) - 2W \end{array}\right] \tag{27}$$

Here, *W*, *X, Y,* and *Z* are constants representing the quadratic time dependence of each surface concentration.

***Third-order expansions*—**For third-order expansions (**Equation (28)**), we apply the cubic formula to solve the resulting polynomials.

$$\mathbf{C} = \mathbf{C}^{\mathbf{o}} + \left(\mathbf{b} - \mathbf{K}\mathbf{C}^{\mathbf{o}}\right)t - \frac{1}{2}\left(\mathbf{K}\mathbf{b} - \mathbf{K}^2\mathbf{C}^{\mathbf{o}}\right)t^2 + \frac{1}{6}\left(\mathbf{K}^2\mathbf{b} - \mathbf{K}^3\mathbf{C}^{\mathbf{o}}\right)t^3 \tag{28}$$

However, to our knowledge, a concise analytical solution does not exist for the logarithm of a third-order polynomial, frustrating a closed-form analytical expression for VE. Accordingly, we leverage numerical integration to compute the average charge and discharge voltages. For completeness, the third-order derivations are provided in the **Supplementary Information** (**SI**).

Computational tools and model implementation—To assess the relative error of the simplified model against the complete analytical solution (**Equation (12)**), we leveraged MATLAB® R2022b; similar to [23], eigenvalues and eigenvectors of **K** were calculated using the *eig* function, nonlinear algebraic equations were solved implicitly using the *fsolve* function, and numerical integration was performed using the *cumtrapz* function. The spreadsheet model used in this work was constructed in Microsoft® Excel® 2021 and leverages straightforward algebraic and matrix operations (i.e., *mmult*, *transpose*). All simulation results presented throughout this work were performed on a Dell Latitude 7290 laptop computer with an Intel® Core™ i7-8650U processor (quad-core, 1.90 GHz) and a random-access memory of 16 GB.

Results and discussion

Assessing error for closed-form approximations—We begin by comparing the accuracy of the closed-form approximations with those obtained using numerical methods reported in reference [23]. As a representative example, **Figure 1** compares discharge capacities using the "Complete 0-D model"—solved using numerical methods—to the second-order closed-form approximations for differing active species diffusion coefficients through the membrane. Note that the cycling conditions used here are analogous to those used to generate Figure 6 in reference [23] and are detailed in **Table S1**. Qualitatively, the second-order approximations capture capacity fade well across a range of crossover rates, highlighting the efficacy of using low-order Taylor expansions to simplify the model equations. However, assessing the relative accuracy of this approach requires a more rigorous evaluation of error across varying model inputs.

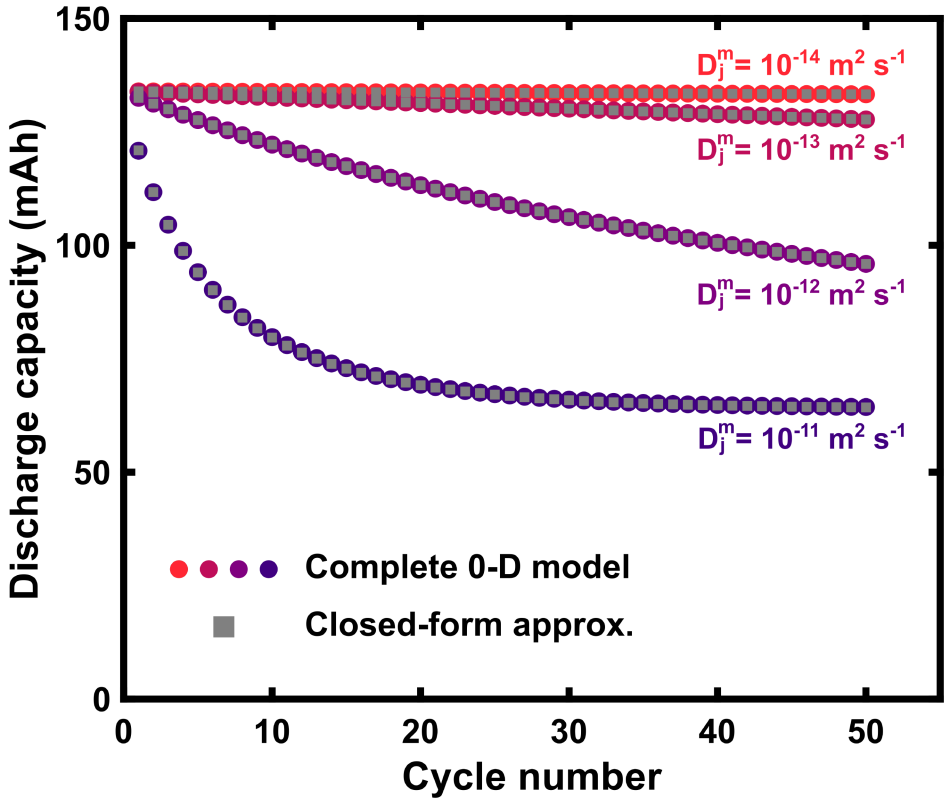

Figure 1. A qualitative comparison of the second-order closed-form approximation to results obtained from the complete zero-dimensional model for different membrane diffusion

coefficients (assumed to be equal for all species). All cell conditions for both sets of data are identical to those reported in Figure 6 of reference [23] and detailed in **Table S1**.

To expedite the process of comparing simulations across a large set of independently tunable input parameters, we employ dimensional analysis to identify and evaluate a reduced set of quantities, shown in **Table 1**. The dimensionless groups represent intrinsic relationships between different process timescales while the dimensional quantities (i.e., OCV, ohmic losses) represent cell energetics. While this form of analysis is not required to implement the modeling framework, it greatly simplifies parametric sweeps and provides bounding on the simplifying assumptions within the closed-form models. For each of these dimensionless groups, we randomly select model inputs across a uniform distribution for physically realistic model conditions and conduct all simulations for 1000 cycles to provide sufficient time for parasitic processes to proceed. However, note that the actual time represented by each cycle depends on the dimensional parameters, meaning that the timescales of the simulation may vary depending on inputs. We quantify error between the "complete 0-D model" and the three closed-form approximations by comparing both parity and RMSE between the capacities and efficiencies predicted by the models. Results were generated using the same computation resources and are reported for 1000 unique parameter combinations, yielding a total of 10^6 data points.

Table 1. Studied parameters and their ranges / values used for comparing model outputs. All terms involving bulk species concentrations are scaled by the initial concentration of A.

Studied parameter	Definition	Ranges / values
Dimensionless charge capacity	$\frac{It_c}{V^+C_A^oF}$	0 – 1
Dimensionless discharge capacity	$\frac{It_d}{V^+C_A^oF}$	0 – 1
Dimensionless current	$\frac{I}{FA_{ed}k_mC_A^o}$	0 – 0.25

OCV (V)	$E^{0,+} - E^{0,-}$	1 – 3
Ohmic losses (V)	$I\left(R_m + R_c\right)$	0 – 0.3
Dimensionless permeability of A	$\frac{D_A^m K_A A_m F C_A^o}{I l_m}$	10^{-7} – 10^{-3}
Dimensionless permeability of B^+	$\frac{D_{B^+}^m K_{B^+} A_m F C_A^o}{I l_m}$	10^{-7} – 10^{-3}
Permeability ratio of A^+	$D_{A^+}^m / D_A^m$	0.1 – 10
Permeability ratio of B	$D_B^m / D_{B^+}^m$	0.1 – 10
Dimensionless electric field	$\frac{F I l_m}{\sigma_m R T A_m}$	10^{-3} – 10
Dimensionless electro-osmotic flux	$\frac{\xi I l_m}{\nu C_{\text{site}} D_j^m A_m}$	0
Dimensionless decay rate of A^+	$\frac{k_{d,A^+} C_A^o V^+ F}{I}$	10^{-7} – 0.01
Dimensionless decay rate of B	$\frac{k_{d,B} C_A^o V^+ F}{I}$	10^{-7} – 0.01
f_{A^+} (–)	---	0.01 – 0.99
f_B (–)	---	0.01 – 0.99
z_A (–)	---	1
z_{B^+} (–)	---	2

Figures 2a, **2b**, and **2c** show parity plots for discharge capacities predicted by first-, second-, and third-order approximations ("predicted values"), respectively, measured against those calculated using the analytical mass balances ("actual values"). As the randomly generated inputs are dimensionless, we report the capacity as a dimensionless fraction of the theoretical capacity. The parity plots display cycling results from 1000 simulations; to aid in interpretation, a single set of simulations (1000 cycles) with the same input parameters is highlighted in red. Compared to the first-order approximation, the second- and third-order approximations describe the solution well over a relatively broad range of input values as indicated by the tight clustering of values around the parity line. The error is further quantified by the RMSE in **Figure 2d** for the

charge and discharge capacities as well as the coulombic, voltaic, and energy efficiencies. Here, we calculate RMSE for each cycling simulation (1000 cycles) and report the average and standard deviation across all parameter combinations (1000 simulations), yielding a total of 10^6 data points. Similar trends are observed with respect to the relative accuracy where < 1% relative error is observed for all model inputs beyond the first-order approximation. However, given the wide range of independent parameters, we observe considerable variation in the relative error, especially for the first-order approximation. For instance, the RMSE of the discharge capacity ranges to as low as ca. 10^{-7} and to as high as ca. 0.24. Upon closer inspection, the simulations featuring the largest degree of inaccuracy are those with longer charge / discharge times and faster crossover and decay rates; this error is further exacerbated by significant electric field contributions. Migration causes larger differences in crossover rate constants between charge and discharge, leading to compounding errors from cycle to cycle. These phenomena are reflected in the arcing trajectories in **Figure 2a** that extend from the parity line as cycling proceeds and later converges closer to zero.

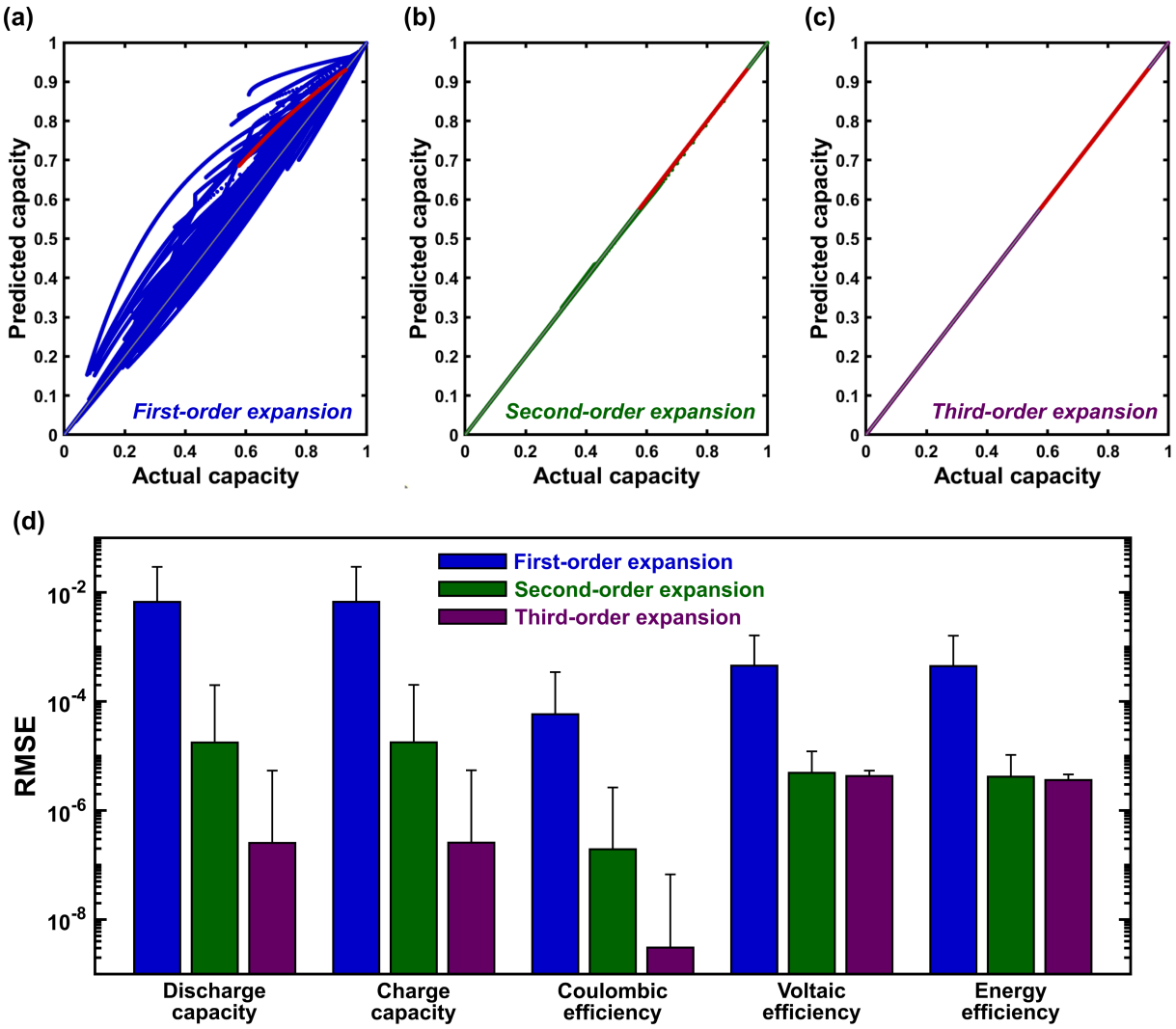

Figure 2. Parity plot comparing dimensionless discharge capacities predicted from closed-form approximations ("predicted capacity") versus those determined from the complete zero-dimensional model ("actual capacity") for (a) first-order expansion, (b) second-order expansion, and (c) third-order expansion. Red traces represent a single simulation (1000 cycles) with identical input parameters. (d) Average root-mean-square error (RMSE) for dimensionless charge and discharge capacities as well as coulombic, voltaic, and energy efficiencies, comparing the values predicted by closed-form approximations with the complete zero-dimensional model. Simulations were conducted over 1000 cycles using randomly generated inputs (**Table 1**) and repeated 1000 times.

As expected, extending the Taylor expansion improves model accuracy, as the higher-order terms better approximate the exponential function at increasing times and with faster decay and crossover rates. This is evinced by both the tighter clustering around the parity line and the lower magnitudes of the RMSE observed in the quantitative analysis. While there exist some

differences between the second- and third-order approximations, the additional accuracy gained is diminishing and does not appear to meaningfully affect results. Further, we reiterate that third-order expansions prohibit the derivation of closed-form expressions for VE and EE and introduce considerable difficulty in identifying the polynomial roots needed to predict charge and discharge capacities. These limitations lead to marked differences in computation time, requiring ca. 3×10^{-5}, 0.001, and 0.05 s per cycle for the first-order, second-order, and third-order expansions, respectively. Thus, we conclude that second-order approximations are sufficient for predicting performance metrics while providing a simple theoretical framework.

An accessible simulation platform in Microsoft® Excel®—A key feature of closed-form analytical expressions is that they enable spreadsheet modeling of redox cells across a range of diagnostic and performance configurations, which could increase accessibility and facilitate integration with pre-existing experimental data processing workflows. Considering the aforementioned tradeoffs between second- and third-order expansions, we elected to leverage the simpler second-order expressions for designing a spreadsheet model. The model is constructed in Microsoft® Excel® 2021 and features a wide range of variable input parameters corresponding to electrolyte, electrode, and membrane properties, cell configuration, and operating conditions. **Figure 3** shows a snapshot of the prototype spreadsheet, featuring the input properties and their descriptions as well as representative outputs. The input values (highlighted in yellow) can be readily adjusted to simulate varying experimental conditions; however, the model is subject to the same assumptions and limitations presented in reference [23] and outlined in the theoretical framework (vide supra). Finally, the cutoff voltages are included to set the voltage at the end of each half-cycle for data visualization and are not used to determine the charge capacity.

Matrix operations are performed in a separate tab of the spreadsheet to compute capacities and efficiencies at each cycle using results from the previous cycle. As a representative case, results are shown for 100 full charge / discharge cycles, however the simulation can be extended by copying and pasting rows of the calculations tab. For select cycles—by default, cycles 1, 10, 20, 40, 60, 80, 100—the time-dependent concentrations and cell voltage are also calculated in separate spreadsheet tabs at multiple time points (i.e., 1000) throughout each half-cycle to compute charge / discharge voltage profiles. The selected cycles can be changed by altering the input cycle numbers.

As expected from the earlier error analysis, the results here are consistent with those obtained using the complete zero-dimensional model. Accordingly, the accuracy of this model as compared with experimental cells is subject to the validity of the overarching zero-dimensional assumption (e.g., low single-pass conversion, well-mixed electrolytes). As already noted, prior low-dimensional models have reported suitable accuracy for capturing charge / discharge behavior in vanadium RFBs[26,28] and aqueous organic RFBs,[24] and our previous experimental results show quantitative agreement for membrane characterization.[19] Importantly, charge/discharge capacities, cell voltages, and cycling efficiencies can be simulated in ca. 1 s after updating input parameters, meaning that variables can be readily manipulated to explore relationships between material properties and performance outputs. Additionally, the spreadsheet model may also enable facile performance predictions prior to and during cycling experiments, allowing for test planning and real-time comparisons between measured characteristics and expected results.

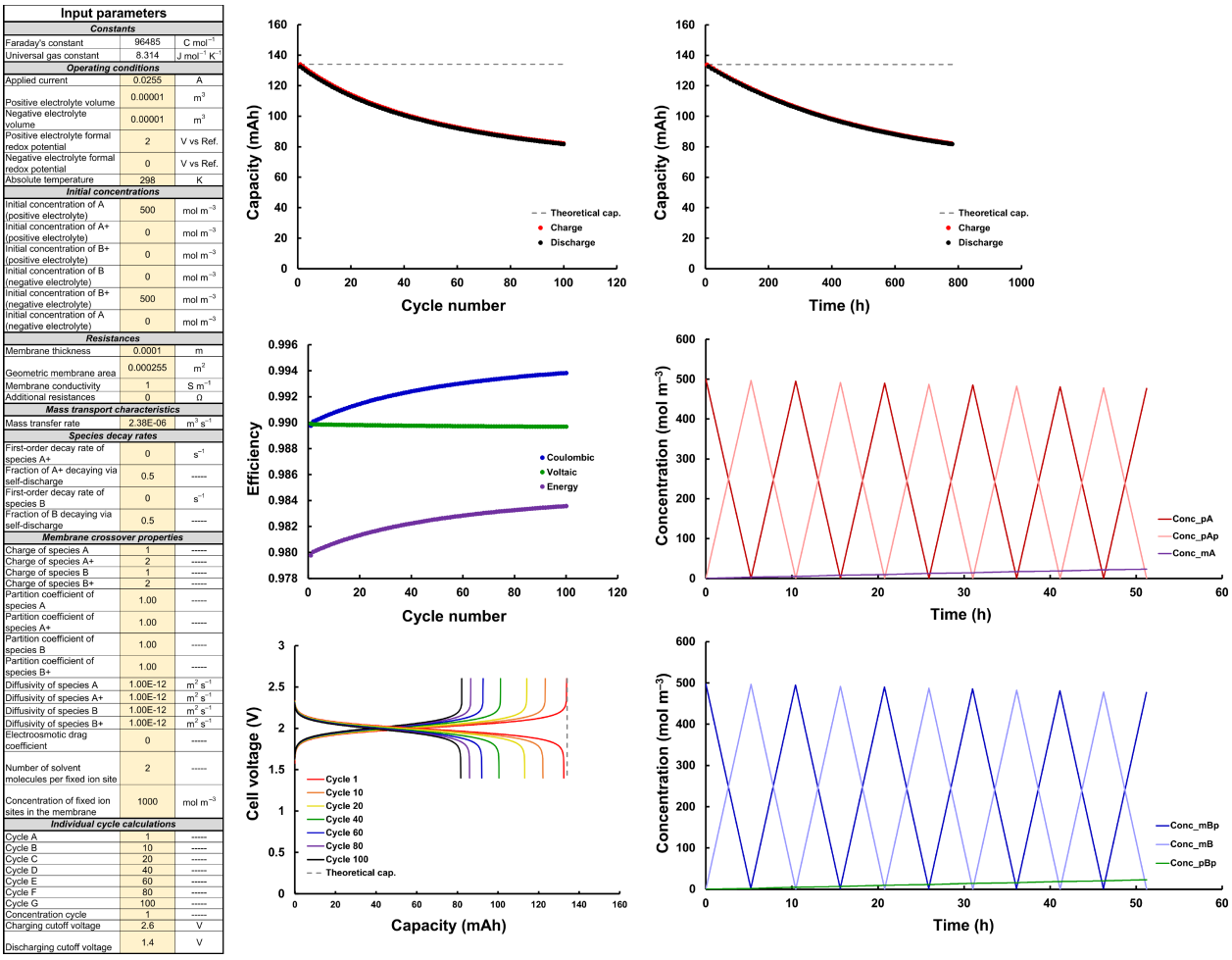

Figure 3. Screenshot of the zero-dimensional spreadsheet model constructed in Excel® 2021, showing simulation representative inputs and performance metrics.

***Exploring model utility through retrospective data analysis*—**We posit that this spreadsheet tool may find broad utility in complementing analysis and experimental planning for cell cycling. As such, we aim to illustrate several possible uses of the model by retrospectively analyzing cycling data published by our group and others. We focus here on our own results to maintain consistency across this work and because we have easy access to the raw experimental data. In doing so, we apply the model to three distinct experimental configurations—bulk electrolysis, compositionally unbalanced symmetric cell cycling (CUSCC), and full cell cycling—highlighting its flexibility. In each instance, we compare predictions from the spreadsheet model with experimental data and discuss how this tool can be leveraged to augment such studies in the future. For all model results shown here, the parameters used for each set of simulations is provided in **Section S2** of the **SI**.

First, we consider work by Kowalski et al. that investigated the impact of bulk electrolysis cycling conditions on measured capacity fade rates for 2,5-di-tert-butyl-1,4-bis(2-methoxyethoxy)benzene (DBBB) in propylene carbonate containing 1 M lithium bistriflimide (LiTFSI).[39] Because bulk electrolysis evaluates a single electrolyte—with the counter-electrode chamber containing lithium metal in this case—we approximate the negative half-cell as a large excess volume at 50% state-of-charge ($V^{-} = 1$ m^3, $C_{B^+}^{\infty,-} = 1$ mol m^{-3}, $C_{B}^{\infty,-} = 1$ mol m^{-3}) such that it does not impact capacity, similar to a volumetrically unbalanced compositionally symmetric cell.[18,40] Considering that crossover is likely to proceed through the porous glass frit separating the counter electrode chamber from the working electrode chamber, we estimate the crossover diffusion coefficients and membrane conductivities by assuming they are approximately 20% of their values in the bulk ($D_A^m = 2 \times 10^{-11}$ m^2 s^{-1}, $\sigma_m = 0.05$ S m^{-1}),[41] which has been measured previously for gas diffusion in similar fritted substrates.[42] Mass transfer coefficients are set

explicitly and are estimated based on the limiting current measured prior to cycling (**Section S3**). To estimate decay rates, we leverage results from another work by Kowalski et al. that uses microelectrodes to measure DBBB decay in an identical electrolyte.[43] **Figure 4** compares experimental capacity fade results from Kowalski et al. with those generated by the spreadsheet model, showing reasonable agreement across the range of currents measured, which correspond to rates of 1 C, 0.5 C, 0.25 C, and 0.125 C. Importantly, the relative agreement between decay rates measured via microelectrodes and capacity fade measured via cell cycling further underscores the connections between ex situ properties and predicted electrochemical cell performance. However, we observe some differences between the predicted and experimental data, which we tentatively attribute to temperature fluctuations, incomplete mixing in the bulk electrolysis cell, and incomplete characterization of crossover—for instance, the reaction between DBBB and the lithium counter electrode is not well understood. In retrospect, utilization of this model in conjunction with the bulk electrolysis experiments would have augmented and helped to explain the impact of operating conditions on observed stability. Further, the model could have been used to estimate decomposition rates from capacity fade data, which likely would have agreed well with those measured via complementary ex situ techniques.

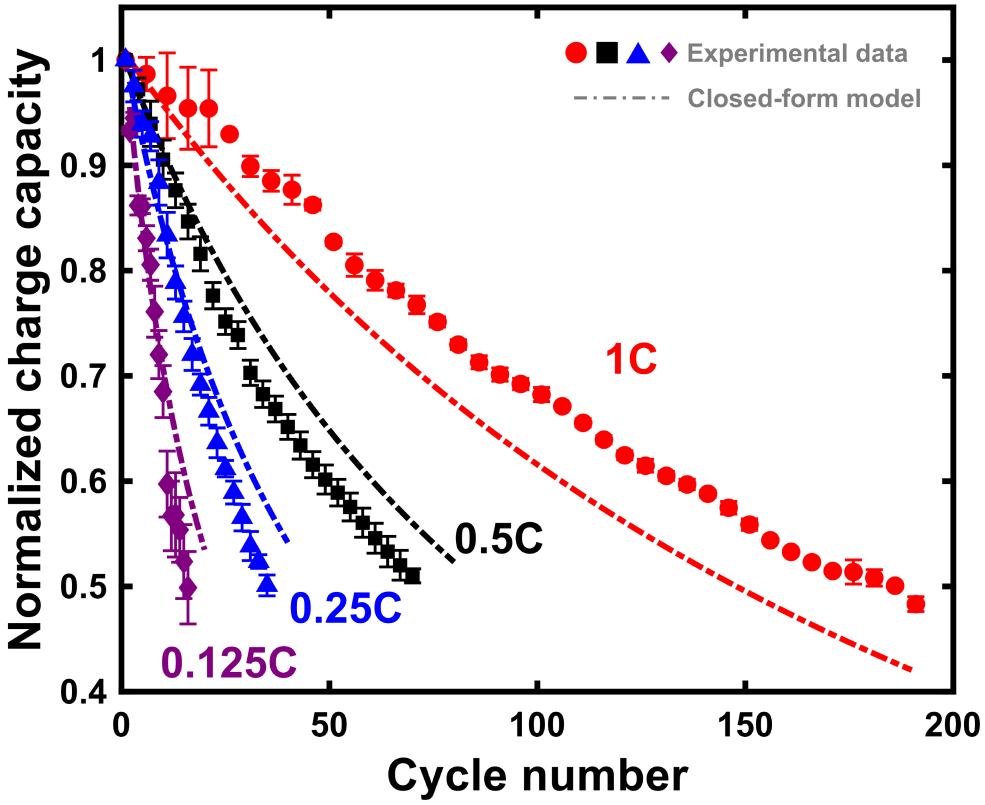

Figure 4. Comparison of capacity fade results measured by Kowalski et al. with those predicted by the spreadsheet model. Data was collected in a bulk electrolysis configuration with 30 mL of 1 mM DBBB and 1 M LiTFSI in propylene carbonate. Charging rates of 1C, 0.5C, 0.25C, and 0.125C correspond to currents of 0.804 mA, 0.402 mA, 0.201 mA, and 0.1005 mA, respectively. Error bars represent the average and standard deviation from two different cells. Data adapted from *Electrochemistry Communications* 2020, 111, 106625 with permission under CC BY 4.0 open access. The closed-form model inputs match the operating conditions of the cell while mass transport characteristics ($A_{ed}k_{m,j}$) were estimated from the cell limiting current. Decay rates ($k_{d,A^+} = 9.9 \times 10^{-6}$ s^{-1} and $f_{A^+} = 0.87$) were estimated from [43] as described in the **Section S3**.

Next, we evaluate our recent work describing a technique for measuring crossover in redox flow cells using CUSCC.[19] This study uses a symmetric cell configuration, requiring modification of the model to include a single active species in either half-cell. The modified mass balance is shown in **Equation (29)**, and the general solution strategy outlined above still

applies. Solutions for the charge / discharge times are analogous to **Equations (25)** and **(26)** with matrix indices adjusted to account for the modified mass balances.

$$\frac{d}{dt}\begin{bmatrix} C_A^{\infty,+} \\ C_{A^+}^{\infty,+} \\ C_A^{\infty,-} \\ C_{A^+}^{\infty,-} \end{bmatrix} = \begin{bmatrix} -\frac{I}{V^+F} \\ \frac{I}{V^+F} \\ \frac{I}{V^-F} \\ -\frac{I}{V^-F} \end{bmatrix} - \begin{bmatrix} k_{c,A}^+ & -f_{A^+}k_{d,A^+} & -k_{c,A}^- & 0 \\ 0 & k_{d,A^+}+k_{c,A^+}^+ & 0 & -k_{c,A^+}^- \\ -\frac{V^+}{V^-}k_{c,A}^+ & 0 & \frac{V^+}{V^-}k_{c,A}^- & -f_{A^+}k_{d,A^+} \\ 0 & -\frac{V^+}{V^-}k_{c,A^+}^+ & 0 & k_{d,A^+}+\frac{V^+}{V^-}k_{c,A^+}^- \end{bmatrix} \begin{bmatrix} C_A^{\infty,+} \\ C_{A^+}^{\infty,+} \\ C_A^{\infty,-} \\ C_{A^+}^{\infty,-} \end{bmatrix} \quad (29)$$

Note that in **Equation (29)**, we maintain the positive and negative half-cell notation for consistency with earlier forms of the mass balances, but there should not be a potential difference between the electrolytes at equilibrium. Neyhouse et al. used the aqueous $FeCl_2$ / $FeCl_3$ redox couple as a chemically stable model system; thus, we again assume that species decay rates are negligible. All other parameters are identical to those reported in reference [19] and detailed in **Table S3**. **Figure 5** compares experimental capacity gain data reported by Neyhouse et al. with results obtained by our spreadsheet model. As expected, the model results agree well with experimental data; however, it is important to note that the input parameters used here were obtained by least-squares fitting in the original work; hence, as the closed-form model agrees well with the complete zero-dimensional model, quantitative agreement should be consistent with that obtained in reference [19]. We posit that it would also have been possible to start with parameters measured using ex situ techniques (i.e., H-cell crossover, membrane conductivity) and manually tune them to improve data fitting. While rigorous parameter estimation may be difficult in Excel®, this tool provides a means to interpret experimental data and predict cycling behavior more easily. For instance, we could have used this tool in place of the complete zero-dimensional model to develop intuition for the factors that underscore capacity gain. Similarly,

we also could have used the spreadsheet model alongside ex situ data to identify the most suitable operating conditions for experimental validation. Beyond CUSCC, this implementation of the model can also be applied to conventional symmetric cells,[18,44] enabling predictions of species decay—similar to bulk electrolysis—and facilitating judicious consideration of cycling conditions and their impact on perceived capacity fade.

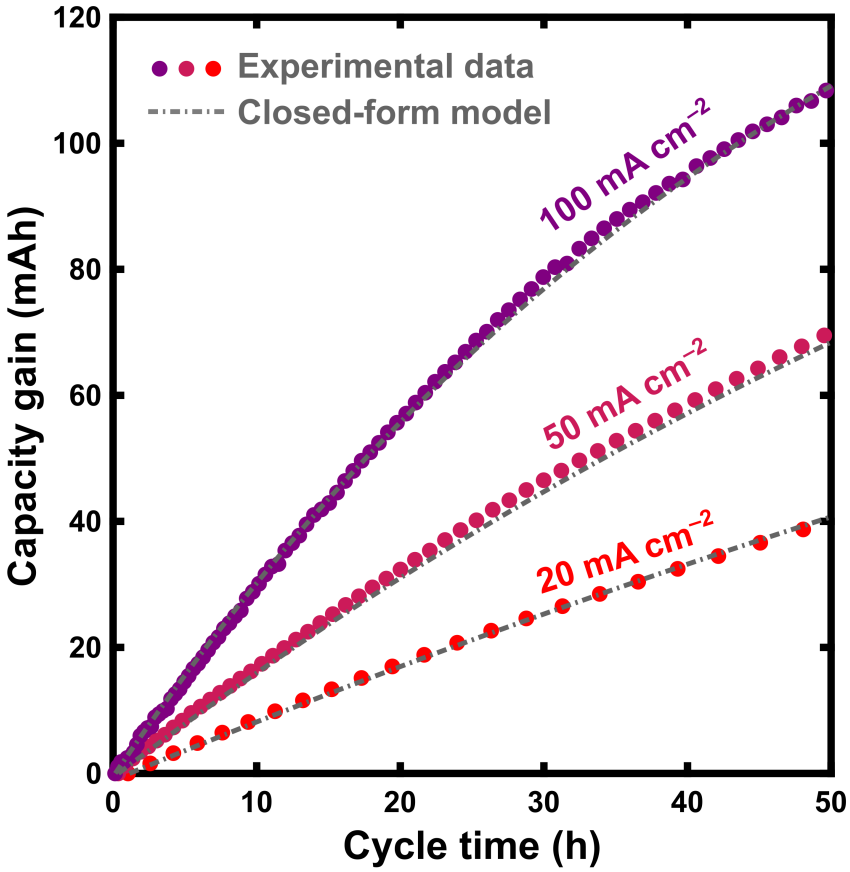

Figure 5. Comparison of CUSCC capacity gain results measured by Neyhouse et al. with those predicted by the spreadsheet model. Data was collected in a 2.55 cm^2 flow cell featuring a Nafion 117 membrane, carbon paper electrodes, interdigitated flow fields, and 15 mL of electrolyte in each half-cell. The donor electrolyte (positive electrolyte) initially contains 0.5 M $FeCl_2$ and 0.5 M $FeCl_3$ in 2 M HCl. The receiver electrolyte (negative electrolyte) initially contains 0.05 M $FeCl_2$, 0.05 M $FeCl_3$, 0.45 M $MgCl_2$, and 0.45 M $CrCl_3$ in 2 M HCl. Data adapted from *ChemRxiv* with permission under CC BY NC ND 4.0 open access. The closed-form model inputs match the operating conditions of the cell while mass transport characteristics and membrane properties are taken from the best-fit parameters reported in [19].

Finally, we evaluate results reported by Liang et al., using model phenothiazine and viologen derivatives—N-[2-(2-methoxyethoxy)ethyl]phenothiazine (MEEPT) and bis[2-(2-methoxyethoxy)ethyl] viologen bistriflimide (MEEV-$TFSI_2$) in acetonitrile with 0.5 M tetraethylammonium tetrafluoroborate ($TEABF_4$) supporting electrolyte—to assess the role of the membrane / separator on nonaqueous cell cycling.[45] This work employs a conventional full cell configuration that is consistent with the base model and requires no modifications. In addition to the reported experimental parameters for cell cycling, we initially estimate membrane permeabilities and conductivities from crossover and cell resistance data, and then further refine those values using the *goal seek* function in Excel® (**Section S2**). As negligible active species loss was observed in post mortem analysis, we assume decay rates for both species are zero. **Figure 6** compares results from the spreadsheet model with those measured experimentally, showing good agreement for capacity fade and cycling efficiencies. While the "fit" appears more accurate than our earlier comparison to Kowalski et al., it is worth noting that, here, we are fitting only one data set. Importantly, the model captures the decrease in capacity below the theoretical capacity for fully mixed electrolytes as shown earlier by Small et al. in an aqueous organic RFB.[46] That is, while one might initially expect the capacity to approach equilibrium at half the original theoretical capacity, we instead observed continuous capacity fade below this value resulting from electric-field-driven crossover. Both Liang et al. and Small et al. only offer qualitative explanations of this phenomenon based on a fundamental understanding of membrane transport, however access to this model enables more robust and quantitative data interpretation. Notably, prediction of this trend would have likely been possible based solely on properties measured using ex situ techniques (i.e., voltammetry, H-cell crossover, membrane area-specific resistance).

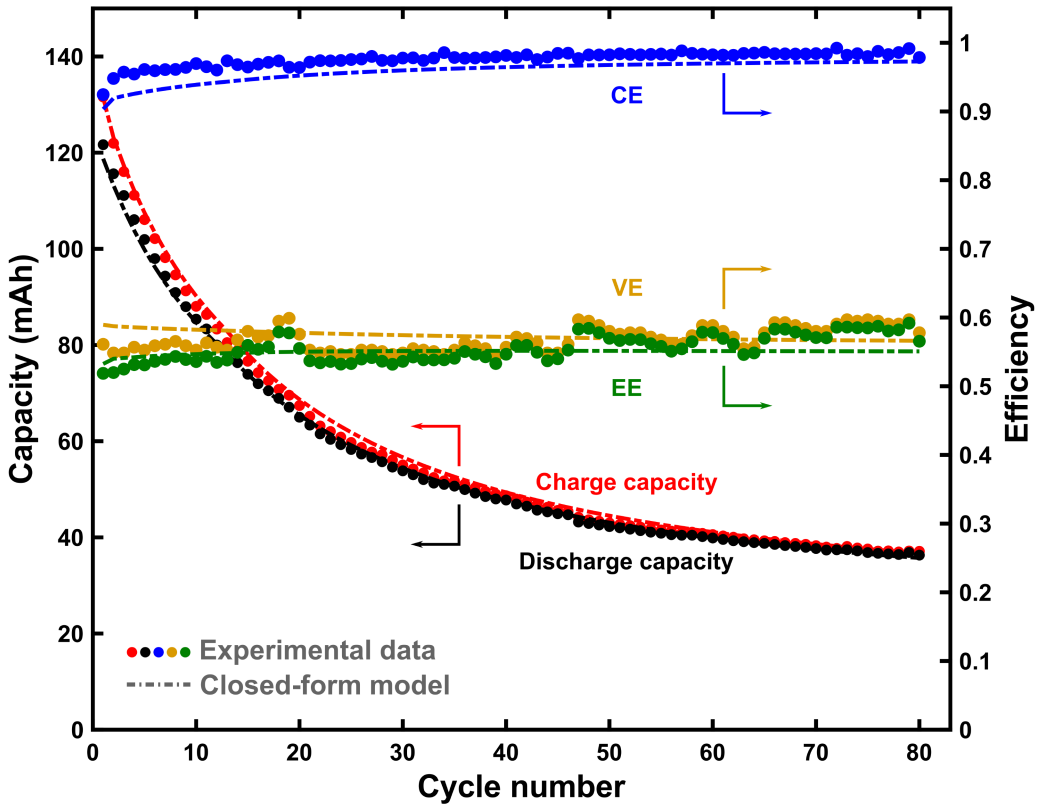

Figure 6 Comparison of cell cycling results measured by Liang et al. with those predicted by the spreadsheet model. Data was collected in a 2.55 cm^2 flow cell featuring 2× FAPQ 375 PP membranes, carbon paper electrodes, interdigitated flow fields, and 10 mL of electrolyte in each half-cell. The positive electrolyte initially contains 0.5 M MEEPT and 0.5 M $TEABF_4$ in acetonitrile. The negative electrolyte initially contains 0.5 M MEEV-$TFSI_2$ and 0.5 M $TEABF_4$ in acetonitrile. Adapted with permission from *ACS Applied Energy Materials*, 4, 6, 5443–5451. Copyright 2021 American Chemical Society. The closed-form model inputs match the operating conditions of the cell while mass transport characteristics and membrane properties are estimated from the experimental data as described in **Sections S2** and **S3**.

Conclusions

In this work, we have developed closed-form expressions for cell cycling performance, leveraging Taylor expansions to approximate solutions to the coupled species mass balances. By comparing the RMSE between these approximations and the complete analytical solution, we determined that the second-order expansion is sufficiently accurate for predicting cell cycling performance under practically relevant experimental conditions. Further, such low-order approximations enable facile numerical implementation, allowing us to develop a spreadsheet modeling package in Microsoft® Excel®. We applied this model to retrospectively analyze published data from our group and others, demonstrating its utility for complementing data analysis for cell configurations common in the published literature, including bulk electrolysis, compositionally unbalanced symmetric cell cycling, and full cell cycling.

More generally, this work seeks to further establish and advance zero-dimensional models for RFB development. Specifically, the rapid computation times afforded by this framework and similar models may aid in broader computation analyses, including optimization, controls, and techno-economic evaluations. The accessibility of this particular framework and the associated spreadsheet application may also find utility in electrochemical engineering education, complementing undergraduate curricula and guiding new entrants to the RFB field. Indeed, we have previously employed these models in undergraduate electrochemical engineering courses as a learning exercise in analyzing representative RFB performance and failure modes. Although widely used, we note that Excel® may not be accessible to all researchers; however, the mathematical framework that enables this spreadsheet model can be readily implemented in other open-access spreadsheet tools and programming languages.

CRediT authorship contribution statement

Bertrand J. Neyhouse: Conceptualization, Methodology, Software, Validation, Investigation, Data curation, Visualization, Writing – original draft, Writing – review and editing. **Fikile R. Brushett**: Conceptualization, Project administration, Supervision, Writing – original draft, Writing – review and editing.

Acknowledgements

This work was supported as part of the Joint Center for Energy Storage Research, an Energy Innovation Hub funded by the U.S. Department of Energy, Office of Science, Basic Energy Sciences. B.J.N gratefully acknowledges financial support from the Martin Family Society of Fellows for Sustainability as well as from the NSF Graduate Research Fellowship Program under Grant Number 2141064. Any opinion, findings, and conclusions or recommendations expressed in this material are those of the authors and do not necessarily reflect the views of the NSF. We also thank Dr. Jessica Tami (McNeil Group, University of Michigan) and Brianna Jett (Sanford Group, University of Michigan) for providing valuable feedback on the spreadsheet model.

List of symbols

Roman symbols

A_{ed}	Accessible electrode surface area (m^2)
A_m	Geometric membrane area (m^2)
$\mathbf{b}$	Constant reaction rate vector (mol m^{-3} s^{-1})
$\mathbf{C}$	Bulk concentration vector (mol m^{-3})
$\mathbf{C^o}$	Initial concentration vector (mol m^{-3})
$C_j^{\infty,h}$	Bulk concentration of species j in half-cell h (mol m^{-3})
$C_j^{o,h}$	Initial concentration of species j in half-cell h at the beginning of each half-cycle (mol m^{-3})
C_j^s	Surface concentration of species j (mol m^{-3})
C_{site}	Concentration of fixed ion sites in the membrane (mol m^{-3})
CE	Fractional coulombic efficiency
D_j^m	Diffusion coefficient of species j in the membrane (m^2 s^{-1})
$E^{0,h}$	Formal redox potential in half-cell h (V)
E_{cell}	Cell voltage (V)
$\bar{E}_c$	Average charging voltage (V)
$\bar{E}_d$	Average discharging voltage (V)
EE	Fractional energy efficiency
f_j	Fraction of species j that decays via self-discharge
F	Faraday constant (96485 C mol^{-1})
I	Applied current, denoted as positive for charging and negative for discharging (A)
$k_{c,j}^h$	Crossover rate constant for species j in half-cell h (s^{-1})
$k_{d,j}$	Decay rate constant for species j (s^{-1})
$k_{m,j}$	Mass transfer coefficient for species j (m s^{-1})
$\mathbf{K}$	Rate constant matrix (s^{-1})
K_j	Membrane partition coefficient for species j
l_m	Swollen membrane thickness (m)
n	Summation index
OCV	Open-circuit voltage (V)
R	Universal gas constant (8.314 J mol^{-1} K^{-1})
R_c	Additional contact resistances (Ω)
R_j^h	Source term for species j in half-cell h (mol m^{-3} s^{-1})
R_m	Membrane ohmic resistance (Ω)

t	Time (s)
t_c	Charge time (s)
t_d	Discharge time (s)
T	Temperature (K)
V^h	Total electrolyte volume in half-cell h (m^3)
VE	Fractional voltaic efficiency
W	Representative constant
x_n	Representative constant
X	Representative constant
Y	Representative constant
Z	Representative constant
z_j	Ionic charge of species j

Greek symbols

γ_j	Dimensionless transport parameter for species j
λ	Molar ratio of solvent to fixed ion sites in the membrane
ξ	Dimensionless electro-osmotic coefficient
σ_m	Membrane conductivity (S m^{-1})

References

1. J. Yuan et al., *J. Power Sources*, **500**, 229983 (2021).

2. J. A. Kowalski, L. Su, J. D. Milshtein, and F. R. Brushett, *Curr. Opin. Chem. Eng.*, **13**, 45–52 (2016).

3. M. Li, Z. Rhodes, J. R. Cabrera-Pardo, and S. D. Minteer, *Sustain. Energy Fuels*, **4**, 4370–4389 (2020).

4. D. G. Kwabi, Y. Ji, and M. J. Aziz, *Chem. Rev.*, **120**, 6467–6489 (2020).

5. F. R. Brushett, M. J. Aziz, and K. E. Rodby, *ACS Energy Lett.*, **5**, 879–884 (2020).

6. S.-H. Shin, S.-H. Yun, and S.-H. Moon, *RSC Adv.*, **3**, 9095–9116 (2013).

7. L. Zhang, R. Feng, W. Wang, and G. Yu, *Nat Rev Chem*, **6**, 524–543 (2022).

8. Y. A. Gandomi et al., *J. Electrochem. Soc.*, **165**, A970 (2018).

9. H. Wang et al., *ACS Nano*, **14**, 2575–2584 (2020).

10. M. Li et al., *ACS Energy Lett.*, **6**, 3932–3943 (2021).

11. B. J. Neyhouse and F. R. Brushett, in *Encyclopedia of Energy Storage*, L. F. Cabeza, Editor, p. 453–465, Elsevier, Oxford (2022) https://www.sciencedirect.com/science/article/pii/B9780128197233000585.

12. J. Schneider, T. Tichter, and C. Roth, in *Flow Batteries*, p. 229–262, John Wiley & Sons, Ltd (2023) https://onlinelibrary.wiley.com/doi/abs/10.1002/9783527832767.ch11.

13. D. Aaron, Z. Tang, A. B. Papandrew, and T. A. Zawodzinski, *J. Appl. Electrochem.*, **41**, 1175–1182 (2011).

14. C. Zeng et al., *J. Electrochem. Soc.*, **169**, 120527 (2022).

15. R. Darling, K. Gallagher, W. Xie, L. Su, and F. Brushett, *J. Electrochem. Soc.*, **163**, A5029–A5040 (2016).

16. M. L. Perry, J. D. Saraidaridis, and R. M. Darling, *Curr. Opin. Electrochem.*, **21**, 311–318 (2020).

17. R. M. Darling, A. Z. Weber, M. C. Tucker, and M. L. Perry, *J. Electrochem. Soc.*, **163**, A5014 (2015).

18. M.-A. Goulet and M. J. Aziz, *J. Electrochem. Soc.*, **165**, A1466 (2018).

19. B. J. Neyhouse, R. M. Darling, J. D. Saraidaridis, and F. R. Brushett, *J. Electrochem. Soc.*, **170**, 080514 (2023).

20. O. C. Esan et al., *Adv. Energy Mater.*, **10**, 2000758 (2020).

21. B. Kumar Chakrabarti et al., *Sustain. Energy & Fuels*, **4**, 5433–5468 (2020).

22. B. J. Neyhouse, A. M. Fenton Jr., and F. R. Brushett, *J. Electrochem. Soc.*, **168**, 050501 (2021).

23. B. J. Neyhouse, J. Lee, and F. R. Brushett, *J. Electrochem. Soc.*, **169**, 090503 (2022).

24. S. Modak and D. G. Kwabi, *J. Electrochem. Soc.*, **168**, 080528 (2021).

25. S. Bogdanov et al., *J. Energy Storage*, **57**, 106191 (2023).

26. M. Pugach, M. Kondratenko, S. Briola, and A. Bischi, *Appl. Energy*, **226**, 560–569 (2018).

27. B. Silcox, J. Zhang, I. A. Shkrob, L. Thompson, and L. Zhang, *J. Phys. Chem. C*, **123**, 16516–16524 (2019).

28. S. B. Lee et al., *J. Electrochem. En. Conv. Stor*, **17** (2020).

29. A. Pathak, A. K. Sharma, and A. K. Gupta, *J. of Energy Storage*, **44**, 103258 (2021).

30. M. Kapoor, R. K. Gautam, V. K. Ramani, and A. Verma, *Chem. Eng. J.*, **379**, 122300 (2020).

31. A. Tang, J. Bao, and M. Skyllas-Kazacos, *J. Power Sources*, **196**, 10737–10747 (2011).

32. A. K. Sharma, C. Y. Ling, E. Birgersson, M. Vynnycky, and M. Han, *J. Power Sources*, **279**, 345–350 (2015).

33. P. A. Boettcher, E. Agar, C. R. Dennison, and E. C. Kumbur, *J. Electrochem. Soc.*, **163**, A5244 (2015).

34. K. Amini et al., *J. Electrochem. Soc.*, **170**, 120535 (2023).

35. J. L. Barton, J. D. Milshtein, J. J. Hinricher, and F. R. Brushett, *J. Power Sources*, **399**, 133–143 (2018).

36. X. You, Q. Ye, and P. Cheng, *J. Electrochem. Soc.*, **164**, E3386 (2017).

37. R. M. Darling and M. L. Perry, *J. Electrochem. Soc.*, **161**, A1381 (2014).

38. A. M. Pezeshki, R. L. Sacci, G. M. Veith, T. A. Zawodzinski, and M. M. Mench, *J. Electrochem. Soc.*, **163**, A5202 (2015).

39. J. A. Kowalski, B. J. Neyhouse, and F. R. Brushett, *Electrochem. Comm.*, **111**, 106625 (2020).

40. I. A. Volodin et al., *ACS Appl. Energy Mater.*, **6**, 302–316 (2023).

41. J. D. Milshtein et al., *J. Electrochem. Soc.*, **164**, A2487–A2499 (2017).

42. Y. Kim and J. T. Gostick, *Int. J. Heat and Mass Transf.*, **129**, 1023–1030 (2019).

43. J. A. Kowalski, A. M. Fenton Jr., B. J. Neyhouse, and F. R. Brushett, *J. Electrochem. Soc.*, **167**, 160513 (2020).

44. E. M. Fell and M. J. Aziz, *J. Electrochem. Soc.*, **170**, 100507 (2023).

45. Z. Liang et al., *ACS Appl. Energy Mater.*, **4**, 5443–5451 (2021).

46. L. J. Small, H. D. Pratt, and T. M. Anderson, *J. Electrochem. Soc.*, **166**, A2536 (2019).